MIT Open Access Articles

Potential energy landscape activations governing plastic flows in glass rheology

Massachusetts Institute of Technology

Potential energy landscape activations governing plastic flows in glass rheology

Penghui Cao[a,b,1], Michael P. Short[c], and Sidney Yip[c,d]

[a]Department of Mechanical and Aerospace Engineering, University of California, Irvine, CA 92697; [b]Department of Materials Science and Engineering, University of California, Irvine, CA 92697; [c]Department of Nuclear Science and Engineering, Massachusetts Institute of Technology, Cambridge, MA 02139; and [d]Department of Materials Science and Engineering, Massachusetts Institute of Technology, Cambridge, MA 02139

While glasses are ubiquitous in natural and manufactured materials, the atomic-level mechanisms governing their deformation and how these mechanisms relate to rheological behavior are still open questions for fundamental understanding. Using atomistic simulations spanning nearly 10 orders of magnitude in the applied strain rate we probe the atomic rearrangements associated with 3 characteristic regimes of homogeneous and heterogeneous shear flow. In the low and high strain-rate limits, simulation results together with theoretical models reveal distinct scaling behavior in flow stress variation with strain rate, signifying a nonlinear coupling between thermally activated diffusion and stress-driven motion. Moreover, we find the emergence of flow heterogeneity is closely correlated with extreme values of local strain bursts that are not readily accommodated by immediate surroundings, acting as origins of shear localization. The atomistic mechanisms underlying the flow regimes are interpreted by analyzing a distance matrix of nonaffine particle displacements, yielding evidence of various barrier-hopping processes on a fractal potential energy landscape (PEL) in which shear transformations and liquid-like regions are triggered by the interplay of thermal and stress activations.

metallic glass | mechanism | atomistic modeling | rheology

Solid materials deform and flow in response to external mechanical loading and thermal relaxation. Compared to crystalline solids, whose plastic flow is governed by topological defects such as dislocations (1), deformation mechanisms of amorphous solids are less well understood due to their inherently amorphous nature (2). It is generally accepted that shear transformation, where a cluster of atoms embedded in an elastic matrix undergoes inelastic rearrangements (3, 4), is responsible for the loss of structural stability in athermal quasistatic deformation (5). Through long-range strain fields (6), a local distortion would trigger other nearby shear transformation events (7) to give rise to avalanche behavior (8), eventually leading to shear banding (9). The accumulation of these plastic events is considered to be related to the shear localization and macroscopic failure of amorphous solids (10).

Besides mechanical stress, thermally activated processes are also key to understanding the rheological behavior in deformed glasses. Amorphous materials typically display complex relaxation spectra (11, 12) consisting of distinct peaks with different relaxation mechanisms (13, 14). From a potential energy landscape viewpoint, the slow α process is identified as a hopping event escaping a metabasin, whereas the β process corresponds to activation across subbasins within an inherent metabasin (12, 14, 15). The elementary barrier hopping in the β process is argued to have comparable activation energy with that required to trigger shear transformation events (13, 15–18), which plays an important role in the physical properties of aging, rejuvenation, diffusion, and mechanical ductility (14, 19).

The interplay of mechanical stress and thermal activation brings about intriguing rheological behaviors in many glassy materials, ranging from metallic to colloidal glasses (19, 20). One important factor in deformation experiments is the strain rate, which directly affects thermally activated barrier hopping occurring within a certain time window by virtue of controlling relaxation processes to occur. Discontinuity in particle diffusion has been observed when shearing colloidal glasses at a critical strain rate, indicating a transition from homogeneous to inhomogeneous flow (21). Similar strain-rate–dependent results in a microscale glass (22) as well as bulk metallic glasses close to the glass transition temperature have been reported (23, 24), showing a cross-over from a ductile behavior at low strain rates to brittle response at increased strain rates. For example, a microscale glass exhibits a homogeneous to inhomogeneous plastic flow transition with increasing strain rate to 6 s^{-1} (22). Detailed analysis of the coupling effects between mechanical stress and thermal activation has been studied in numerous molecular dynamics (MD) simulations (25–27), although the typical strain rates attainable using MD are several orders of magnitude higher than those in laboratory tests. At these high strain rates (typically larger than 10^7 s^{-1}) in MD simulations, slow thermal activation processes are significantly limited only to small barrier activation associated with the short time window or crossing of barriers which have been greatly reduced by the applied stress. Because major thermal relaxations are suppressed due to the short timescale of MD simulations, direct comparison with experiments cannot be easily performed.

In this study a metadynamics algorithm of sampling transition-state pathways is used to simulate the rheological response of a model metallic glass over a strain-rate range of about 10 orders of magnitude (*Materials and Methods*). We consider a model system of $Cu_{50}Zr_{50}$ in 2D with a size of 20 nm $\times$ 20 nm.

Significance

Glassy materials exhibit striking rheological behavior in response to varying external stimuli such as strain rate. Understanding the microscopic processes governing the nature of nonlinear flow is of longstanding interest in the glass community. Here, atomistic simulations of a model metallic glass over an extraordinarily wide range of strain rate reveal distinct local rearrangements both in time and in space, underlying liquid-like and solid-like mechanical responses mediated by strain rate. The spatial and temporal evolution of local strain and single-particle displacement is interpreted in terms of coupled stress activation and thermal hopping on a fractal potential energy landscape. Our results on nonlinear rheology, avalanches, and atomic rearrangements shed light on the commonalities of plastic flows in glass systems.

Interatomic interactions are described through a Lennard-Jones potential (28) which has been used to characterize plastic deformation (29) and thermally activated flows (30). The initial glassy structure is obtained by quenching a high-temperature equilibrated liquid at a slowest possible cooling rate of 0.005 K/ps using MD. We then apply pure shear deformation up to a nominal strain of 50% at prescribed constant strain rates (*Materials and Methods*). The temperature is chosen to be $0.75\,T_g$, which is high enough to bring about significant thermal activation effects in competition with those resulting from mechanical stress, but well below T_g because thermal diffusion-mediated homogeneous flow is known to be predominant at high temperatures (19, 25).

Results

Strain-Rate–Mediated Rheological Responses. The effects of strain rate on mechanical response are illustrated by the stress–strain curves at 4 typical shear rates shown in Fig. 1*A*. An overall lowering of the stress response is readily seen as the shear rate is decreased. For strain rates $6.1 \times 10^4\,\mathrm{s}^{-1}$ and higher, the shear deformation is essentially elastic up to the onset of yielding, followed by serrated plastic flow in the form of stress relaxation events (avalanches). It is interesting to note when reducing the strain rate from $6.1 \times 10^4\,\mathrm{s}^{-1}$ to $20\,\mathrm{s}^{-1}$ the initial elastic behavior disappears and the discrete stress relaxation events merge into a more continuous spectrum. Comparing the stress–strain curves at the highest and lowest strain rates, the mechanical stress response goes from a typical rigid solid to a liquid-like material, indicating a characteristic strain-rate–mediated rheological behavior of the glassy system, requiring physical interpretation in terms of the underlying atomic mechanisms. Fig. 1*B* shows a magnification of the stress–strain curves for the shear strain range 18% to 32%. To identify the stress drop size, the stress–strain curves are smoothed (yellow curve) through median filtering with a bin size of $\delta\gamma = 0.2\%$

(31). Fig. 1*C* presents statistical analysis of the stress drop size $\delta\sigma$, in which the complementary cumulative distribution function (CCDF) $F(\delta\sigma)$ is presented. For strain rates higher than $1.1 \times 10^3\,\mathrm{s}^{-1}$, the $\delta\sigma$ demonstrates a power-law scaling $\propto \delta\sigma^{-0.5}$ for small $\delta\sigma$ spanning 1 order of magnitude. The power exponent, which corresponds to 1.5 for the probability density distribution, has been reported in many studies of stress-driven amorphous solids (32–34), where the plastic deformation proceeds through slip avalanches. At a slow strain rate of $20\,\mathrm{s}^{-1}$, the stress drop sizes take on significantly smaller values and the statistical distribution of $\delta\sigma$ clearly deviates from power-law scaling, suggesting that the plastic flow is not governed by avalanche dynamics.

Strain-Rate Dependence of Flow Stress. Fig. 2*A* shows the variation of steady-state flow stress τ with strain rate $\dot{\gamma}$ from $2.8\,\mathrm{s}^{-1}$ to $5 \times 10^{10}\,\mathrm{s}^{-1}$, where metadynamics simulation results and high strain-rate MD simulations are denoted as black open diamonds and green solid circles, respectively. With increasing shear rate, the flow stress τ displays a growth trend, consisting of 3 characteristic shear-flow regimes, henceforth referred as regimes I, II, and III. In regime I, one finds a power-law relation between stress and shear rate $\tau \propto \dot{\gamma}^m$, with exponent $m = \partial\log(\tau)/\partial\log(\dot{\gamma})$ being the strain rate sensitivity. At the low strain rates in regime I, m is estimated to be 0.75. As $\dot{\gamma}$ increases, τ grows sublinearly on entering into regime II, with m decreasing to ~ 0.12, signifying a weakening strain-rate dependence of flow stress. In regime III a flow stress upturn occurs as indicated in both metadynamics and our own MD simulations (Fig. 2*B*), as well as in previous MD studies (25).

To interpret the strain-rate variation of flow stress in a metallic glass system, we consider theoretical descriptions based on assumed molecular mechanisms of plastic deformation in amorphous materials. At low stresses and strain rates, it is reasonable to assume that thermally activated atomic diffusion governs the plastic flow. Under a small shear stress τ, atom diffusion due to barrier hopping is biased along the shear direction. A conventional diffusional plasticity model gives rise to a scaling behavior between τ and $\dot{\gamma}$ as $\tau \propto A\sinh^{-1}(\dot{\gamma}/B)$, where A and B are material and temperature constants (*Materials and Methods*). As shown in Fig. 2*A*, this inverse hyperbolic dependence of τ on $\dot{\gamma}$ describes the flow stress behavior well in the limit of low strain rate, thus confirming the diffusional nature of regime I. On the other hand, even if the diffusional model predicts strain-rate–mediated flow behavior change, the diffusional mechanism by itself is not adequate to describe the transition behavior from regime I to regime II. The disparity indicates that, apart from diffusion, some other processes such as stress-induced strain burst could be triggered in the onset of regime II. Indeed, stress-induced activations are expected to be the dominant processes at the opposite limit of high $\dot{\gamma}$ and τ (regime III). If the stress-driven shear transformation is considered to be the elementary process governing plastic deformation, the dependence of τ on $\dot{\gamma}$ can be derived as $\tau \propto -C[\ln(D/\dot{\gamma})]^{2/3}$ with material- and temperature-dependent constants C and D (*Materials and Methods*). The scaling relation between τ and $\dot{\gamma}$, stemming from the stress-triggered shear transformation event, conforms to the stress upturn seen in the simulations (Fig. 2*B*).

Spatial and Temporal Evolution of Strain and Displacement. During plastic deformation and flow, atoms must rearrange themselves to accommodate the increase of applied strain. The evolution of local strain fields can proceed in a homogeneous or heterogeneous manner depending on external stimuli such as the strain rate. We examine the molecular trajectories in the simulations and reveal spatial and temporal fluctuations of the local atomic strain as well as individual atom displacements to
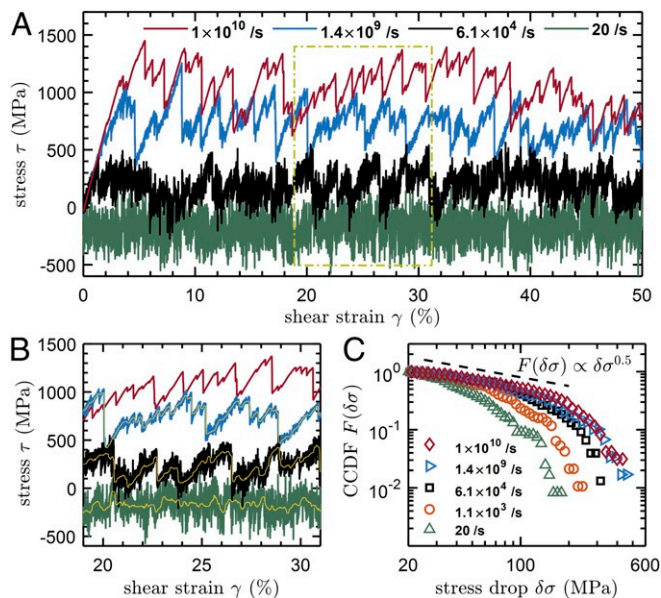
Fig. 1. Effects of strain rate on the mechanical response to shear deformation. (*A*) Stress–strain curves at 4 typical strain rates, 1×10^{10}, 1.4×10^9, 6.1×10^4, and $20\,\mathrm{s}^{-1}$. It should be noted the curve for $20\,\mathrm{s}^{-1}$ has been shifted vertically downward by 200 MPa to facilitate visual inspection. (*B*) Enlargement of *A* from 18% to 32% strain. Yellow lines represent the smoothed stress–strain curves for identifying the stress drop event. (*C*) Complementary cumulative distribution function $F(\delta\sigma)$ for different strain rates. The dashed line indicates power-law scaling $\propto \delta\sigma^{-0.5}$.

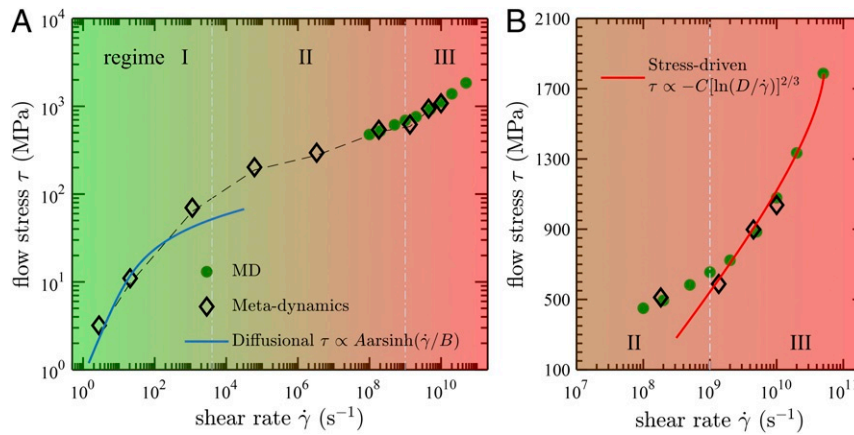**Fig. 2.** Shear rate $\dot{\gamma}$ dependence of steady-state flow stress τ and their scaling relationship. (*A*) Variation of flow stress with shear rate displaying 3 characteristic flow regimes, denoted as I, II, and III. Black open diamonds and green solid circles are data obtained from metadynamics simulations and high strain-rate MD, respectively. At low strain rates, a diffusional model predicts flow stress τ scaling with $\dot{\gamma}$ as $\propto A \sinh^{-1}(\dot{\gamma}/B)$, indicated by the blue solid line. (*B*) Variation of τ with $\dot{\gamma}$ in regime III, with the red solid line indicating the scaling relation $\tau \propto -C[\ln(D/\dot{\gamma})]^{2/3}$ predicted by a stress-driven plasticity model.

identify the deformation processes associated with the different flow regimes. Fig. 3*A* shows the local strain η maps (35) at 50% applied shear strain for the 3 representative shear rates as labeled. For a shear rate of 20 s^{-1}, the majority of atoms in the system are found to participate in plastic deformation, which concurs with the expectation of diffusion-mediated homogeneous flow in the low shear-rate regime I. With increasing shear rate through 3.4×10^6 s^{-1} and 4.5×10^9 s^{-1}, the system exhibits a clear propensity toward the onset of flow inhomogeneity. The flow field at 3.4×10^6 s^{-1} may be described as "patchy" or having the appearance of strain-localized regions embedded in elastically deformed surroundings (Fig. 3*A*, *Center*). At 4.5×10^9 s^{-1} shear flow is seen to be concentrated almost entirely in a banded region of large plastic strain. We resolve the detailed evolution of local strain η during shear flow, and Fig. 3*B* presents its probability distributions at various stages of applied strain γ for strain rate 20 s^{-1}. As expected, the magnitude of atomic strain η grows with increasing γ. Interestingly, when η is rescaled by its mean value $\langle\eta\rangle$, the data points collapse onto a single curve (Fig. 3*B*, *Inset*). This implies that at low strain rates the atoms are able to rearrange themselves to maintain the system in a state of uniform-like strain distribution. For high strain rates, we find the population of large η increases, distorting the uniformity of strain field (*SI Appendix*, Fig. S4), conceivably acting as the origin for the onset of localization or inhomogeneous flow. To uncover its correlation with flow heterogeneity, we apply the extreme value theory (EVT) (36) to analyze the feature of extreme local strain bursts η_{xm} (the tail behavior in the distribution of η) in steady-state flow and how it varies with strain rate. The η_{xm} distributions, obtained by the block maxima approach (37) (*Materials and Methods*), are shown in Fig. 3*C*. At a low shear rate of 20 s^{-1}, the extreme strain burst η_{xm} is about 5 times the system average $\langle\eta\rangle$. With increasing strain rate, η_{xm} grows in magnitude such that the peak of $\eta_{\mathrm{xm}}/\langle\eta\rangle$ reaches 12 with a long tail stretching to 40 at 4.5×10^9 s^{-1}. When a large local strain occurs, it makes the surroundings less able to accommodate the deformation if there is not enough time (for example, if the strain rate is too high to allow thermal relaxation for energy dissipation), and thus shear localization can be triggered. One therefore expects shear localization to give rise to shear-band formation, manifesting as inhomogeneous or heterogeneous flow.

Strain-rate–induced flow cross-over can also be seen from the evolution of atom displacement or flow profiles (*SI Appendix*, Fig. S5). Fig. 3*D* shows scatter plots of each atom's displace-

ment $d\mathrm{x}$ as a function of its location y. From $\dot{\gamma} = 20$ s^{-1} to 4.5×10^9 s^{-1}, a change from a linear profile to a bifurcated one can be seen. In the latter, flow is clearly localized near the upper part of the system while the lower part behaves more like an elastic solid. The nonaffine part of atom displacement, $\delta\mathrm{x}$, is computed by tracking the trajectory of individual atoms and removing the affine displacement as a result of the applied strain. Fig. 3*E* shows the probability distribution $p(\delta\mathrm{x})$ for strain rate 20 s^{-1} where the solid lines indicate best-fit Gaussian functions. Displacement distributions with a Gaussian core and non-Gaussian tails have been ascribed to systems showing dynamic heterogeneity (38). It can be seen that the non-Gaussian tails become broader with increasing shear strain γ that indicates more atoms are involved in nonaffine displacements with increased participation ratio (39). The deviation from Gaussian behavior becomes more pronounced at high strain rate and stress (*SI Appendix*, Fig. S6) as a consequence of stress-induced shear transformation events.

Nonaffine Distance Matrix and Fractal Potential Energy Landscape. Given that varying the strain rate is equivalent to changing the time interval controlling the likelihood of activations on a potential energy landscape (PEL), we can exploit this equivalence to demonstrate a connection between barrier-hopping activations and corresponding atomic rearrangements. In particular we have in mind to probe the interplay between thermal barrier hopping and the effects of stress activation through the strain-rate dependence of flow. To correlate a particular barrier crossing with its corresponding PEL activation event, we define a nonaffine distance matrix (NaDM)

$$\Delta^2(\gamma', \gamma'') = \frac{1}{N} \sum_i^N |\mathbf{R}_i(\gamma'') - \mathbf{F}\mathbf{R}_i(\gamma')|^2, \quad [1]$$

where $\mathbf{R}_i(\gamma')$ is the position of atom i at shear strain γ', and the deformation gradient tensor $\mathbf{F}$ is related to the linear affine transformation from γ' to γ''. For simple shear deformation, $\mathbf{F}$ can be expressed as $\mathbf{F} = 1 + (\gamma'' - \gamma')\mathbf{e_1} \otimes \mathbf{e_2}$, where $\mathbf{e_1}$ and $\mathbf{e_2}$ are basis vectors. Here NaDM is analogous to the distance matrix (40, 41) which has been used to identify basin crossing due to thermal activation. The NaDM provides a measure of the averaged squared nonaffine displacement of a system in a strain interval between γ' and γ'', providing a way to elucidate barrier crossing in mechanical deformation. Note that if the deformation from γ' to γ'' is linearly elastic, the resultant
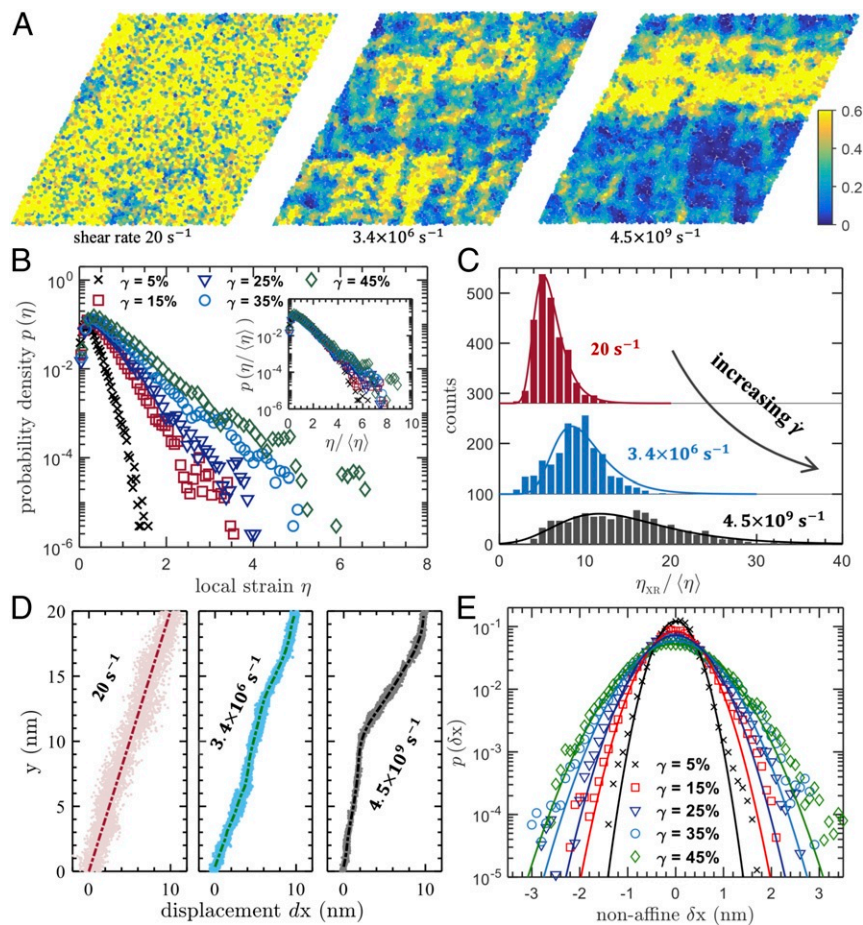
Fig. 3. Spatial and temporal evolution of local atomic strain and displacement during shear flow. (*A*) Local strain η maps at applied strain $\gamma = 50\%$ for 3 characteristic strain rates of 20 s^{-1} (low), 3.4 $\times 10^6$ s^{-1} (intermediate), and 4.5 $\times 10^9$ s^{-1} (high). (*B*) Statistical distributions of local strain η at various applied strains for strain rate 20 s^{-1}. *Inset* shows the distributions normalized by mean value $\langle \eta \rangle$. (*C*) Extreme value analysis of local strain η showing the dependence of strain extremes $\eta_{xr}/\langle \eta \rangle$ on shear rate $\dot{\gamma}$. (*D*) Flow profiles at $\gamma = 50\%$ for the 3 different shear rates indicated. Each data point represents an atom's displacement and the dashed lines indicate flow profiles. (*E*) Statistical distributions of nonaffine displacement δx for strain rate 20 s^{-1}. The solid lines are the best-fit Gaussians.

NaDM would have 0 value, because any local plastic rearrangement due to stress activation or diffusional hopping would cause a finite nonaffine displacement field. In identifying individual barrier hopping and a basin-crossing event, we choose the positions **R** at the local minima of the PEL, known as the inherent structure (12), along the activation trajectory, which should minimize distortion due to effects of thermal vibration.

In Fig. 4*A*, we show a typical NaDM diagram $\Delta^2(\gamma', \gamma'')$ with respect to 2 strains γ' and γ'' for shear rate 2.8 s^{-1}. One can see a clustering of darkly shaded (blue) squares, within which the inherent structures are close to each other. There also exist relatively larger squares which are lightly shaded and in which the dark squares are embedded. Note that by magnifying the dark regions, as shown in Fig. 4*B*, one finds more small shaded blocks appearing and block-to-block crossings which correspond to transitions among the inherent structures (local PEL minima). Comparing the structures of NaDM at different levels reveals self-similar features which we regard as significant evidence of the fractal-like nature of the correlation function NaDM (see *SI Appendix*, Figs. S7 and S12 for details). The structure of the NaDM graph suggests that the potential energy basin has a rough bottom consisting of small minima, and the system experiences dozens of local minima before finding a pathway to escape a current basin and jump into an adjacent one. The mul-

tilevel (hierarchical) aspect of PEL indicated by NaDM can be clearly discerned by computing the averaged squared nonaffine displacement (ASNaD) $\delta^2(\gamma, \xi) = \Delta^2(\gamma - \xi/2, \gamma + \xi/2)$ which corresponds to the quantity along the diagonal of the NaDM over strain lapse ξ at strain γ. Fig. 4*C* shows the ASNaD $\delta^2(\gamma, \xi)$ for 2 different strain rates with ξ that is smaller than the typical strain interval of basin escape, but large enough to include individual local minimum hopping events. The $\delta^2(\gamma, \xi)$ in Fig. 4*C*, *Upper* corresponding to Fig. 4*A* for strain rate 2.8 s^{-1} signifies the jumps between basins manifesting as distinct peaks. The typical value of ASNaD involved in basin hopping is around 0.1, which is compatible with the value of 0.2 in basin transitions of supercooled binary liquids (41). Between the large peaks, the curve with serrated pattern indicates crossing a series of small local minima. The local minimum crossing is prevalent for high strain-rate deformation. For example, the ASNaD for the shear rate of 1×10^{10} s^{-1}, shown in Fig. 4*C*, *Lower*, reveals only small discrete peaks, corresponding to crossings over local minima. It can also be seen that the ASNaD value between peaks is nearly 0. This can be interpreted as the system deforming elastically before saddle-point activation and relaxation into a new local minimum, which triggers plastic events of shear transformation and nonaffine atomic rearrangements in the form of small peaks on the ASNaD curve (*SI Appendix*, Fig. S8). For a large system, various local rearrangement events can occur simultaneously and
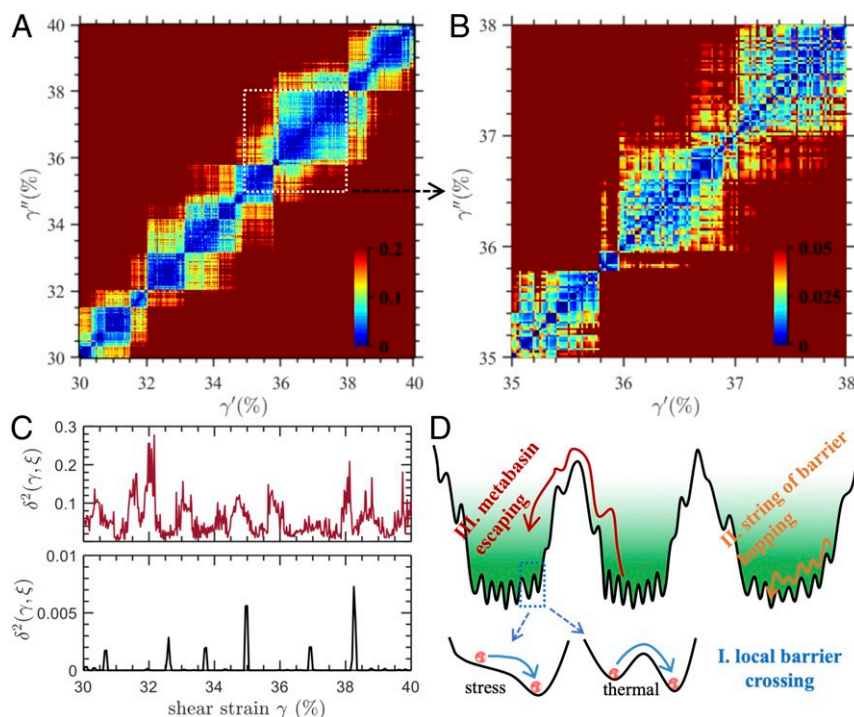
Fig. 4. NaDM and ASNaD associated with barrier hopping on a PEL. (*A*) NaDM $\Delta^2(\gamma', \gamma'')$ for inherent structures visited sequentially during steady-state flow at strain rate 2.8 s^{-1}. (*B*) Enlargement of data in the dashed white window in *A* with scale change shown in key. (*C*) ASNaD $\delta^2(\gamma, \xi)$ at 2 extreme strain rates, 2.8 s^{-1} (*Upper*) and 1×10^{10} s^{-1} (*Lower*). (*D*) Schematic of a fractal-like PEL and 3 barrier activation processes within a metabasin and between metabasins.

sequentially during deformation. If such local events overlap, they would smear out the small peaks in the ASNaD and the local structures of the distance matrix. Therefore a subsystem of 150 atoms is considered here to identify individual local minimum transitions.

In Fig. 4*D*, we depict a schematic scenario of multilevel energy barriers to suggest how certain quantitative features of the NaDM can be interpreted as PEL activations. At a constant temperature, the strain rate plays the role of the order parameter governing the dominant mechanism of barrier hopping on the PEL, for instance what aspects of the landscape are being visited. Based on our findings, we identify 3 types of strain-rate–dependent activation processes: crossing of an individual local barrier, a sequence of small barrier crossings, and a metabasin escape. The activation of a local barrier can result in the loss of local structural stability in the form of a shear transformation (ST) event. It retains an athermal nature even at finite temperature if the deformation is stress dominated, particularly at high strain rates.

To reveal the atomistic mechanisms underlying the 3 characteristic types of energy barrier hopping, we consider the atomic plastic strain and plastically deformed clusters resulting from these activations. Fig. 5*A* shows the spatial distribution of severely rearranged clusters when the system crosses over a local energy barrier (associated with a small peak on the ASNaD). The appearance of isolated events of a cluster of atoms undergoing plastic deformation signifies a stress-induced ST event (*SI Appendix*, Fig. S11) (5). As deformation evolves further, neighboring shear transformations can be triggered in an autocatalytic manner biased in the direction of shear. The accumulation of plasticity events leads to formation of a shear band-like region, and the growth and sliding of such region may lead to macroscopic localized shear flow (42). The second type of hopping involves a series of concerted local barrier activations within a broad PEL basin (metabasin). This could

occur at intermediate strain rates, when the system has more time to pass through many local minima. In Fig. 5*B*, we show the atomistic mechanisms when a string of barrier activations occurs (associated with a series of small peaks on the ASNaD). It can be seen that various processes are triggered, including a cascade of shear transformations and extended shear transformations as a result of local elastic cage breakup (*SI Appendix*, Fig. S11). The third type of activation is related to the escape from one metabasin to an adjacent one, which is a process central to the dynamics of the glass transition (43). When a metabasin hopping occurs (i.e., crossing over a large peak on the ASNaD), a high concentration of liquid-like sites is activated and they percolate throughout the system (Fig. 5*C*). We found for metabasin activation the atoms have activation probability 0.62 which is above the bond percolation threshold of 0.50 (44), indicating a spanning cluster should exist (*SI Appendix*, Fig. S11). The percolation of these activated soft spots therefore underpins the homogeneous-like flow that is characteristic of the shear response at flow regime I. Recalling the previous discussion of the transition from solid to liquid-like behavior in connection with Fig. 1 as modulated by decreasing the strain rate, the mechanism illustrated in Fig. 5*C* provides an explanation of the behavior of shear-induced fluidization in slowly deformed materials (45), dominated by thermally activated particle diffusion.

Discussion

Theoretical models considering various molecular mechanisms have been proposed to address the issue of inhomogeneous plastic flow in metallic glasses, for example free-volume assisted atomic diffusion (46), stress-induced shear transformation (5), and flow defect of STZs (47). The relevance of each model in terms of its ability to quantitatively describe the 3 flow regimes can now be examined, along with how their description can be integrated into stress and thermal activations from the PEL
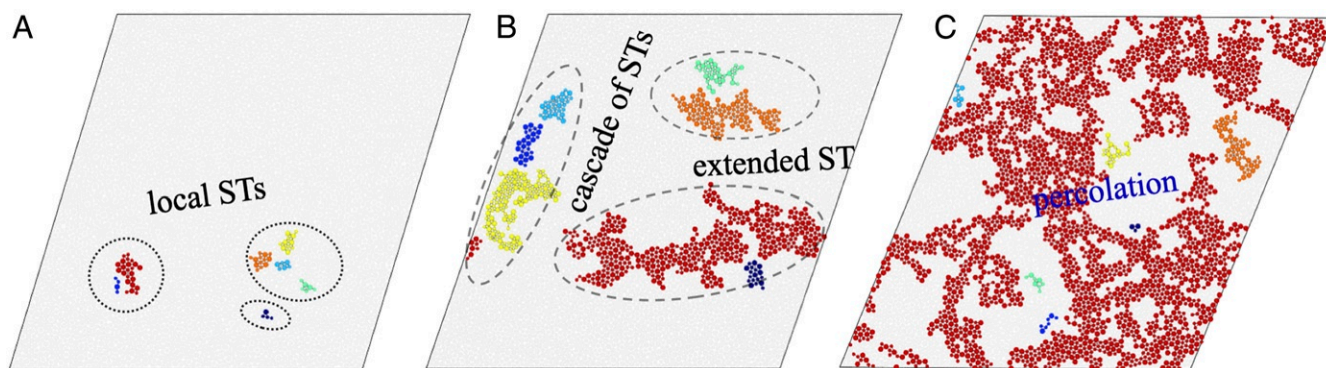
Fig. 5. Spatial distributions of severely plastic deformed clusters for the 3 characteristic types of barrier hopping. (*A*) Local barrier activation involving localized STs. (*B*) A string of correlated barrier hopping leading to extended STs and a cascade of events. (*C*) Metabasin escaping resulting in percolation of highly rearranged (liquid-like) regions and an emerging spanning cluster. The 7 largest clusters are shown whose constituent atoms have plastic strains greater than 10%. The clusters are color coded by size with dark red representing the largest.

perspective. Our results suggest the predominant process in regime I is the percolation of liquid-like spots via thermally activated diffusion and primarily shear-transformation deformation in regime III. In regime II thermal and mechanical activations significantly influence each other and are likely to be strongly coupled. While this study focuses on the strain-rate–mediated rheological behaviors at a constant temperature below the glass transition, it would be interesting to ask how the flow regime cross-overs vary with temperature; this deserves further investigation. Nevertheless, it is anticipated that at a lower temperature the shear rates for the cross-overs would shift to smaller values, because the hopping time for an event to occur will exponentially increase when decreasing the temperature. At a high temperature above the glass transition, it is reasonable to speculate that the cross-over from regime I to II may be vanishing, as the system is away from a fractal deep metabasin containing a collection of subbasins, a feature which is regarded as a root cause of the rheological behavior of glassy materials (48).

In the PEL scenario, the local processes of deformation and diffusion appear as saddle-point activations in the evolving system. While the detailed physical nature of the barriers involved depends on the specific phenomenon under discussion, it is clear that accommodating the mechanisms governing different responses will require a framework of multilevel energy basins and associated nesting of saddle points inherent in a topologically complex surface. For example, the landscape scenario plays a significant role in understanding the fundamental nature of glass transitions as illustrated by the phenomenon of temperature variations of shear viscosity of supercooled liquids (43, 49, 50). Deep in the glass state, it is believed there exists a roughness transition suggested by Gardner (51) in connection with phase transitions in spin glasses. This transition has been discussed theoretically for structural glasses using a disordered ensemble of hard spheres, leading to the interpretation of a metabasin breaking into a fractal hierarchy of subbasins (52). The fractal feature of the energy landscape has been predicted to exist in other glass materials such as soft materials (48), which is considered to be the cause of complex behavior of glassy materials. Our perspective on the PEL is based on the features of NaDM and ASNaD, and by performing a scaling analysis we obtain estimates of the fractal dimension of 1.69 and 1.36, respectively (*SI Appendix*, Fig. S12 and its discussion). Since the NaDM and ASNaD reflect different measures of the underlying PEL, we may regard this finding to suggest both basin area and its associated barrier height can exhibit the fractal feature in a metabasin. The results also suggest that exploring the fractal geometry and hierarchy of the energy landscape provides a perspective

on interpreting anomalous behaviors in glassy materials. For instance, the various barrier events on the fractal PEL (Fig. 4), triggering different processes of shear transformations and liquid-like sites (Fig. 5), virtually dictate the associated atomic rearrangement, avalanches, and rheological behaviors of the glass system.

The rheological behavior mediated by the applied strain rate can be stemming from structural inhomogeneities. Metallic glasses have been depicted to contain soft spots or liquid-like regions, identified from structure information such as quasi-localized low-frequency modes (53, 54), as well as from flexibility volume by combing static free volume with atomic vibrations (55). These soft regions or geometrically disfavored motifs from atomic packing are susceptible to rearrangement and show strong correlation with activation of shear transformation under mechanical deformation (56). Depending on the defined scale of "softness," it could be argued that the distribution of soft regions in a metallic glass system can be spatially localized or percolated. The population of activated soft sites in mechanical loading, which depends on strain rate and temperature, is responsible for the mechanical property heterogeneity, for example homogeneous vs. localized plastic flow. For a small strain increment at a high strain rate or athermal static deformation, only a few shear transformation events can be triggered on the soft sites, inducing extreme large local strains. At intermediate strain rates, thermal activation and the associated atomic diffusion could extend the size of the stimulated site or cause a string of soft-spot activation, and the strained energy can be dissipating out in a more spread-out field. When the strain rate is further lowered, the coupling of thermal activation and stress leads to excitation of a majority of liquid-like regions via collective rearrangements, and if they are percolated through the system, flow in a homogeneous manner would then ensue. We take together the 3 regimes of shear flow and interpret the transitional behavior by the fractal PEL that incorporates the synergistic nature of thermal and stress activations. With the interpretation of the flow regimes through local atomic processes, we give recognition to the interplay between 2 distinct types of atomic rearrangements, the stress-induced shear transformation and the thermally activated process of atomic diffusion. An additional unifying aspect of our perspective is a suggestion to explore the equivalence among the current theoretical studies of amorphous plasticity which are based on seemingly different principles, such as the thermodynamics-based shear transformation zone theory (57), time correlation functions in the self-consistent mode-coupling approximation (58), and variants of mean-field models in condensed-matter theory (59).

Materials and Methods

Molecular Dynamics Simulations. We consider a model $Cu_{50}Zr_{50}$ metallic glass thin film in 2D, in which atoms interact through a binary Lennard-Jones potential (28) previously developed to study mechanical properties of metallic glass. The initial glassy system is produced by quenching an equilibrated high-temperature liquid from 1,000 K down to 0 K at a finite cooling rate of 0.005 K/ps. A metallic glass sample with a dimension of 20 nm × 20 nm is prepared and further relaxed to 0 pressure at the designated temperature 0.75 T_g, where $T_g = 420$ K is the glass transition temperature, in an isothermal–isobaric ensemble using Nose–Hoover-style equations of motion (60). We deform the system in simple shear at constant strain rates ranging from 1×10^8 s^{-1} to 5×10^{10} s^{-1}. The shear strain is imposed on the system by shearing the simulation box in the x direction and remapping the atoms' velocity according to their positions. The shear deformation is performed at constant volume and temperature with periodic boundary conditions applied in all directions, allowing the atoms to cross the boundaries. Three distinct glass samples are created and deformed using MD and metadynamics modeling, resulting in the conclusion of the study (*SI Appendix*, Fig. S10 discussion).

Metadynamics Modeling. The metadynamics simulation algorithm, based on PEL modeling and transition-state theory, was designed to circumvent the timescale limitation of conventional MD (61, 62). It enables investigating the material deformation response at lower strain rates than those intrinsic to MD (42). Specifically, we begin with the system at 0.75 T_g prepared by the same procedure described above. The steepest descent energy minimization (63) is performed to bring the system to the nearest local energy minimum. We then sample activation pathway trajectories starting from the local minimum state by the autonomous basin climbing (ABC) algorithm (64, 65). The PEL sampling algorithm is stopped when an activation barrier greater than a prescribed barrier Q_0 is obtained. A set of transition-state pathway trajectories consisting of a series of local energy minima and saddle points is thus generated. We choose a local minimum state from the sampled local energy minimum states according to the Metropolis algorithm (66) and apply a small shear strain increment 0.0001 to the selected state followed by energy minimization (42). We repeat the activation pathway sampling using the same criterion of barrier Q_0. In such a procedure, the imposed strain rate can be kept constant, which is calculated by $\dot{\gamma} = \dot{\gamma}_0 \exp(-Q/k_B T)$, where k_B is the Boltzmann constant, $Q = (1 - a(T))Q_0$ is the temperature-dependent activation free energy (67), and the parameter $\dot{\gamma}_0$ represents a characteristic strain rate. Given a potential energy barrier Q_0, the effective strain rate depends on parameter $a(T)$ and $\dot{\gamma}_0$ which can be determined by comparing with MD and molecular static (MS) simulations (*SI Appendix*, section 1).

Extreme Value Analysis. From the standpoint of strain localization, a large local strain burst can be more important than the small one because the extreme large one cannot be easily accommodated by the surrounding matrix. Such a spontaneous and highly deformed site could act as an embryo of the shear localized region. To understand the correlation between the tail behavior of local strain distributions (i.e., extreme values) and macroscopic deformation heterogeneity, we apply EVT (36) to probe the feature of extreme values of the underlying local strain η in plastic flow. We use the block maxima approach (37) to extract extreme local strain (*SI Appendix*, section 2). Specifically, the deformation regime is equally separated into p sequences of blocks, and let $\eta_{i,j}$ be the local strain associated with atom j in block i, where index j ranges from 1 to p, and atom index i is from 1 to the total number of atoms in the system. In such a way a p series of block maximum $\eta_{xr}^1, \ldots, \eta_{xr}^i \ldots, \eta_{xr}^p$ is generated, and here $\eta_{xr}^i = \max(\eta_i, j)$ is the extreme value in block i. We use a block size of $\delta\epsilon = 0.5\%$, splitting the entire deformation $\epsilon = 50\%$ into 100 blocks. In each block, the top 10 largest atomic strain values out of 5,000 atoms are picked, which produces a large amount of extreme values for comparing with generalized extreme value (GEV) distributions (*SI Appendix*, Fig. S3). We attain the feature of extreme values from the validated data distributions.

Scaling Relationship between τ and $\dot{\gamma}$. The plastic deformation processes in amorphous solids involve deformational or diffusional or coupling of both mechanisms, and their occurrence depends on the applied strain rate—how fast the system is driven by mechanical stress. At high strain rate $\dot{\gamma}$ and high flow stress τ, thermal barrier hopping can occur only to cross over a small barrier reduced by the applied shear stress. The stress-induced shear transformation event, preserving athermal owing to the limited thermal effects, is considered to be the mechanism underpinning amorphous plasticity (5). Analogous to Orowan's formula in crystalline plasticity (68), the strain rate and activation rate of the shear transformation event can be related as $\dot{\gamma} = \rho_1 c_1 v_0 \exp(-E(\tau)/k_B T)$, where $v_0 \exp(-E(\tau)/k_B T)$ represents the activation rate of the plastic event at stress τ and temperature T, ρ_1 is the density of the potential event site per volume, and c_1 is a constant factor quantifying the contribution of the plastic event to system-level (macroscopic) strain. The energy barrier E, which leads to the activation of a shear transformation event, decreases with shear stress τ, commonly written as $E(\tau) \propto (1 - (\tau/\tau_c)^p)^q$ with shape parameters p and q (69). Here τ_c represents the stress threshold at which the barrier E vanishes. When τ approaches τ_c, E and τ follow a scaling law of $E(\tau) = E_0(1 - \tau/\tau_c)^{3/2}$, where E_0 is the characteristic material-specific barrier (70, 71). Combing the above 2 equations renders the τ and $\dot{\gamma}$ relationship as

$$\tau \propto -C \left[\ln(D/\dot{\gamma})\right]^{2/3} \qquad [2]$$

with $C = \tau_c(k_B T/E_0)^{2/3}$, and $D = \rho_1 c_1 v_0$.

At low strain rate $\dot{\gamma}$ and low stress τ, thermally activated diffusion is considered to play the predominate role in plastic flow (46). For a representative flow unit with volume Ω, the work done by the stress τ on Ω, which undergoes diffusive transformation strain $\delta\eta$, will be $w(\tau, \delta\eta) = \tau\Omega\delta\eta$. Biased by this applied stress, the actual activation rate of the flow unit can be expressed as $v(\tau) = v_0 \exp\left(-\frac{\Delta E_0}{k_B T}\right) \left(\exp\left(\frac{\tau\delta\eta\Omega}{k_B T}\right) - \exp\left(-\frac{\tau\delta\eta\Omega}{k_B T}\right)\right)$, where $v_0 \exp\left(-\frac{\Delta E_0}{k_B T}\right)$ is the activation rate at the stress-free condition, the term $\exp\left(\frac{\tau\delta\eta\Omega}{k_B T}\right)$ measures the accelerated forward-flux rate due to τ, and $\exp(-\frac{\tau\delta\eta\Omega}{k_B T})$ counts the backward flux against τ. Therefore, the $\dot{\gamma}$ and τ are related by $\dot{\gamma} = c_2\rho_2 v_0 \exp\left(-\frac{\Delta E_0}{k_B T}\right) \sinh\left(\frac{\tau\delta\eta\Omega}{k_B T}\right)$, which leads to the scaling relationship as

$$\tau \propto A\sinh^{-1}(\dot{\gamma}/B) \qquad [3]$$

with $B = c_2\rho_2 v_0 \exp(-\Delta E_0/k_B T)$, and $A = k_B T/\delta\eta\Omega$.

1. A. H. Cottrell, B. A. Bilby, Dislocation theory of yielding and strain ageing of iron. *Proc. Phys. Soc. Lond. Sect. A* **62**, 49–62 (1949).
2. T. C. Hufnagel, C. A. Schuh, M. L. Falk, Deformation of metallic glasses: Recent developments in theory, simulations, and experiments. *Acta Mater.* **109**, 375–393 (2016).
3. C. E. Maloney, A. Lemaitre, Amorphous systems in athermal, quasistatic shear. *Phys. Rev. E* **74**, 016118 (2006).
4. A. Tanguy, F. Leonforte, J.-L. Barrat, Plastic response of a 2d Lennard-Jones amorphous solid: Detailed analysis of the local rearrangements at very slow strain rate. *Eur. Phys. J. E* **20**, 355–364 (2006).
5. A. S. Argon, Plastic deformation in metallic glasses. *Acta Metall.* **27**, 47–58 (1979).
6. J. D. Eshelby, The determination of the elastic field of an ellipsoidal inclusion, and related problems. *Proc. R. Soc. Lond. A* **241**, 376–396 (1957).
7. D. Şopu, A. Stukowski, M. Stoica, S. Scudino, Atomic-level processes of shear band nucleation in metallic glasses. *Phys. Rev. Lett.* **119**, 195503 (2017).
8. N. P. Bailey, J. Schiøtz, A. Lemaître, K. W. Jacobsen, Avalanche size scaling in sheared three-dimensional amorphous solid. *Phys. Rev. Lett.* **98**, 095501 (2007).
9. A. L. Greer, Y. Q. Cheng, E. Ma, Shear bands in metallic glasses. *Mater. Sci. Eng. R Rep.* **74**, 71–132 (2013).
10. Y. Shi, M. L. Falk, Strain localization and percolation of stable structure in amorphous solids. *Phys. Rev. Lett.* **95**, 095502 (2005).
11. G. P. Johari, M. Goldstein, Viscous liquids and the glass transition. II. Secondary relaxations in glasses of rigid molecules. *J. Chem. Phys.* **53**, 2372–2388 (1970).
12. P. G. Debenedetti, F. H. Stillinger, Supercooled liquids and the glass transition. *Nature* **410**, 259–267 (2001).
13. D. Pan, A. Inoue, T. Sakurai, M. W. Chen, Experimental characterization of shear transformation zones for plastic flow of bulk metallic glasses. *Proc. Natl. Acad. Sci. U.S.A.* **105**, 14769–14772 (2008).
14. J. S. Harmon, M. D. Demetriou, W. L. Johnson, K. Samwer, Anelastic to plastic transition in metallic glass-forming liquids. *Phys. Rev. Lett.* **99**, 135502 (2007).
15. Y. Fan, T. Iwashita, T. Egami, How thermally activated deformation starts in metallic glass. *Nat. Commun.* **5**, 5083 (2014).
16. Z. Wang, B. A. Sun, H. Y. Bai, W. H. Wang, Evolution of hidden localized flow during glass-to-liquid transition in metallic glass. *Nat. Commun.* **5**, 5823 (2014).

17. D. Rodney, C. A. Schuh, Distribution of thermally activated plastic events in a flowing glass. *Phys. Rev. Lett.* **102**, 235503 (2009).
18. S. G. Mayr, Activation energy of shear transformation zones: A key for understanding rheology of glasses and liquids. *Phys. Rev. Lett.* **97**, 195501 (2006).
19. C. A. Schuh, T. C. Hufnagel, U. Ramamurty, Mechanical behavior of amorphous alloys. *Acta Mater.* **55**, 4067–4109 (2007).
20. L. Berthier, G. Biroli, Theoretical perspective on the glass transition and amorphous materials. *Rev. Mod. Phys.* **83**, 587–645 (2011).
21. V. Chikkadi, D. M. Miedema, M. T. Dang, B. Nienhuis, P. Schall, Shear banding of colloidal glasses: Observation of a dynamic first-order transition. *Phys. Rev. Lett.* **113**, 208301 (2014).
22. R. Ramachandramoorthy et al., Dynamic plasticity and failure of microscale glass: Rate-dependent ductile-brittle-ductile transition. *Nano Lett.* **19**, 2350–2359 (2019).
23. J. Lu, G. Ravichandran, W. L. Johnson, Deformation behavior of the Zr41.2Ti13.8CU12.5Ni10Be22.5 bulk metallic glass over a wide range of strain-rates and temperatures. *Acta Mater.* **51**, 3429–3443 (2003).
24. T. G. Nieh, J. Wadsworth, Homogeneous deformation of bulk metallic glasses. *Scr. Mater.* **54**, 387–392 (2006).
25. J. Chattoraj, C. Caroli, A. Lemaître, Universal additive effect of temperature on the rheology of amorphous solids. *Phys. Rev. Lett.* **105**, 266001 (2010).
26. P. Guan, M. Chen, T. Egami, Stress-temperature scaling for steady-state flow in metallic glasses. *Phys. Rev. Lett.* **104**, 205701 (2010).
27. Y. Q. Cheng, E. Ma, Intrinsic shear strength of metallic glass. *Acta Mater.* **59**, 1800–1807 (2011).
28. S. Kobayashi, K. Maeda, S. Takeuchi, Computer simulation of deformation of amorphous cu57zr43. *Acta Metall.* **28**, 1641–1652 (1980).
29. C. A. Schuh, A. C. Lund, Atomistic basis for the plastic yield criterion of metallic glass. *Nat. Mater.* **2**, 449–452 (2003).
30. D. Rodney, C. Schuh, Distribution of thermally activated plastic events in a flowing glass. *Phys. Rev. Lett.* **102**, 235503 (2009).
31. W. K. Pratt, *Digital Image Processing* (John Wiley and Sons, 1978).
32. J. Antonaglia et al., Bulk metallic glasses deform via slip avalanches. *Phys. Rev. Lett.* **112**, 155501 (2014).
33. J.-O. Krisponeit et al., Crossover from random three-dimensional avalanches to correlated nano shear bands in metallic glasses. *Nat. Commun.* **5**, 3616 (2014).
34. J. Lin, E. Lerner, A. Rosso, M. Wyart, Scaling description of the yielding transition in soft amorphous solids at zero temperature. *Proc. Natl. Acad. Sci. U.S.A.* **111**, 14382–14387 (2014).
35. F. Shimizu, S. Ogata, J. Li, Theory of shear banding in metallic glasses and molecular dynamics calculations. *Mater. Trans.* **48**, 2923–2927 (2007).
36. E. Castillo, *Extreme Value Theory in Engineering* (Elsevier, 2012).
37. A. J. McNeil, *Extreme Value Theory for Risk Managers* (Departement Mathematik, ETH Zentrum, 1999).
38. P. Chaudhuri, L. Berthier, W. Kob, Universal nature of particle displacements close to glass and jamming transitions. *Phys. Rev. Lett.* **99**, 060604 (2007).
39. R. A. Riggleman, H.-N. Lee, M. D. Ediger, J. J. De Pablo, Heterogeneous dynamics during deformation of a polymer glass. *Soft Matter* **6**, 287–291 (2010).
40. I. Ohmine, Liquid water dynamics: Collective motions, fluctuation, and relaxation. *J. Phys. Chem.* **99**, 6767–6776 (1995).
41. G. A. Appignanesi, J. A. Rodriguez Fris, R. A. Montani, W. Kob, Democratic particle motion for metabasin transitions in simple glass formers. *Phys. Rev. Lett.* **96**, 057801 (2006).
42. P. Cao et al., Nanomechanics of slip avalanches in amorphous plasticity. *J. Mech. Phys. Solids* **114**, 158–171 (2018).
43. P. G. Debenedetti, F. H. Stillinger, Supercooled liquids and the glass transition. *Nature* **410**, 259–267 (2001).
44. D. Stauffer, A. Aharony, A. Aharony, *Introduction to Percolation Theory* (Taylor & Francis, 1992).
45. C. Eisenmann, C. Kim, J. Mattsson, D. A. Weitz, Shear melting of a colloidal glass. *Phys. Rev. Lett.* **104**, 035502 (2010).
46. F. Spaepen, A microscopic mechanism for steady state inhomogeneous flow in metallic glasses. *Acta Metall.* **25**, 407–415 (1977).
47. M. L. Falk, J. S. Langer, Deformation and failure of amorphous, solidlike materials. *Annu. Rev. Condens. Matter Phys.* **2**, 353–373 (2011).
48. H. J. Hwang, R. A. Riggleman, J. C. Crocker, Understanding soft glassy materials using an energy landscape approach. *Nat. Mater.* **15**, 1031 (2016).
49. M. Goldstein, Viscous liquids and the glass transition: A potential energy barrier picture. *J. Phys. Chem.* **51**, 3728–3739 (1969).
50. C. A. Angell, Formation of glasses from liquids and biopolymers. *Science* **267**, 1924–1935 (1995).
51. E. Gardner, Spin glasses with p-spin interactions. *Nucl. Phys. B* **257**, 747–765 (1985).
52. P. Charbonneau, J. Kurchan, G. Parisi, P. Urbani, F. Zamponi, Fractal free energy landscapes in structural glasses. *Nat. Commun.* **5**, 3725 (2014).
53. M. L. Manning, A. J. Liu, Vibrational modes identify soft spots in a sheared disordered packing. *Phys. Rev. Lett.* **107**, 108302 (2011).
54. J. Ding, S. Patinet, M. L. Falk, Y. Cheng, E. Ma, Soft spots and their structural signature in a metallic glass. *Proc. Natl. Acad. Sci. U.S.A.* **111**, 14052–14056 (2014).
55. J. Ding et al., Universal structural parameter to quantitatively predict metallic glass properties. *Nat. Commun.* **7**, 13733 (2016).
56. E. Ma, Tuning order in disorder. *Nat. Mater.* **14**, 547–552 (2015).
57. J. S. Langer, Shear-transformation-zone theory of plastic deformation near the glass transition. *Phys. Rev. E* **77**, 021502 (2008).
58. M. Gruber, G. Coelho Abade, A. M. Puertas, M. Fuchs, Active microrheology in a colloidal glass. *Phys. Rev. E* **94**, 042602 (2016).
59. K. A. Dahmen, Y. Ben-Zion, J. T. Uhl, Micromechanical model for deformation in solids with universal predictions for stress-strain curves and slip avalanches. *Phys. Rev. Lett.* **102**, 175501 (2009).
60. S. Nosé, A unified formulation of the constant temperature molecular dynamics methods. *J. Chem. Phys.* **81**, 511–519 (1984).
61. Y. Fan, Y. N. Osetskiy, S. Yip, B. Yildiz, Mapping strain rate dependence of dislocation-defect interactions by atomistic simulations. *Proc. Natl. Acad. Sci. U.S.A.* **110**, 17756–17761 (2013).
62. P. Cao, M. P. Short, S. Yip, Understanding the mechanisms of amorphous creep through molecular simulation. *Proc. Natl. Acad. Sci. U.S.A.* **114**, 13631–13636 (2017).
63. R. Fletcher, M. J. D. Powell, A rapidly convergent descent method for minimization. *Comput. J.* **6**, 163–168 (1963).
64. A. Kushima et al., Computing the viscosity of supercooled liquids. *J. Chem. Phys.* **130**, 224504 (2009).
65. P. Cao, M. Li, R. J. Heugle, H. S. Park, X. Lin, A self-learning metabasin escape algorithm and the metabasin correlation length of supercooled liquids. *Phys. Rev. E* **86**, 016710 (2012).
66. N. Metropolis, A. W. Rosenbluth, M. N. Rosenbluth, A. H. Teller, E. Teller, Equation of state calculations by fast computing machines. *J. Chem. Phys.* **21**, 1087–1092 (1953).
67. T. Zhu, J. Li, A. Samanta, A. Leach, K. Gall, Temperature and strain-rate dependence of surface dislocation nucleation. *Phys. Rev. Lett.* **100**, 025502 (2008).
68. E. Orowan, Problems of plastic gliding. *Proc. Phys. Soc. Lond.* **52**, 8–22 (1940).
69. U. F. Kocks, A. S. Argon, M. F. Ashby, Thermodynamics and kinetics of slip. *Prog. Mater Sci.* **19**, 1–281 (1975).
70. W. L. Johnson, K. Samwer, A universal criterion for plastic yielding of metallic glasses with a $(t/t_g)^{2/3}$ temperature dependence. *Phys. Rev. Lett.* **95**, 195501 (2005).
71. C. E. Maloney, D. J. Lacks, Energy barrier scalings in driven systems. *Phys. Rev. E* **73**, 061106 (2006).